

Time-dependent Hamiltonian estimation for Doppler velocimetry of trapped ions

L. E. de Clercq, R. Oswald, C. Flühmann, B. Keitch, D. Kienzler,
H.-Y. Lo, M. Marinelli, D. Nadlinger, V. Negnevitsky, J. P. Home

Institute for Quantum Electronics, ETH Zürich, Otto-Stern-Weg 1, 8093 Zürich, Switzerland

The time evolution of a closed quantum system is connected to its Hamiltonian through Schrödinger's equation. The ability to estimate the Hamiltonian is critical to our understanding of quantum systems, and allows optimization of control. Though spectroscopic methods allow time-independent Hamiltonians to be recovered, for time-dependent Hamiltonians this task is more challenging [1–6]. Here, using a single trapped ion, we experimentally demonstrate a method for estimating a time-dependent Hamiltonian of a single qubit. The method involves measuring the time evolution of the qubit in a fixed basis as a function of a time-independent offset term added to the Hamiltonian. In our system the initially unknown Hamiltonian arises from transporting an ion through a static, near-resonant laser beam [7]. Hamiltonian estimation allows us to estimate the spatial dependence of the laser beam intensity and the ion's velocity as a function of time. This work is of direct value in optimizing transport operations and transport-based gates in scalable trapped ion quantum information processing [8–10], while the estimation technique is general enough that it can be applied to other quantum systems, aiding the pursuit of high operational fidelities in quantum control [11, 12].

Estimation of the underlying dynamics which drive the evolution of systems is a key problem in many areas of physics and engineering. This knowledge allows control inputs to be designed which account for imperfections in the physical implementation. For closed quantum systems, the time dependence of a system is driven by the Hamiltonian through Schrödinger's equation. If the Hamiltonian is static in time, a wide range of techniques have been proposed for recovering the Hamiltonian [1–3, 13], which have been applied to a variety of systems including chemical processes [4] and quantum dots [5, 6]. These methods often involve estimation of the eigenvectors and eigenvalues of the Hamiltonian via spectroscopy, or through pulse-probe techniques for which a Fourier transform of the time-evolution gives information about the spectrum. However these methods are not directly applicable to time-dependent Hamiltonians. Such Hamiltonians are becoming of increasingly important as quantum engineering pursues a combination of high operational fidelities and speed, often involving fast variation of control fields which are particularly susceptible to distortion before reaching the quantum device [9, 10, 14–17].

In this Letter, we propose and demonstrate a method

for reconstructing a general time-dependent Hamiltonian with two non-commuting terms which drives the evolution of a single qubit. The method works with any single qubit Hamiltonian $\hat{H} = \sum_i f_i(t)\hat{\sigma}_i$, where the $f_i(t)$ are arbitrary time-dependent functions and $\hat{\sigma}_i$ are the Pauli operators. In our experiments, a Hamiltonian with two non-commuting time-dependent terms arises when we try to perform quantum logic gates by transporting an ion through a static laser beam [7, 18]. In this case, the Hamiltonian describing the interaction between the ion and the laser can be written in an appropriate rotating frame as

$$\hat{H}_I(t) = \frac{\hbar}{2} (-\Omega(t)\hat{\sigma}_x + \delta(t)\hat{\sigma}_z) \quad (1)$$

which includes a time-varying Rabi frequency $\Omega(t)$, and an effective detuning $\delta(t)$ which is related to the first-order Doppler shift of the laser in the rest frame of the moving ion (see [19] for details). For a Hamiltonian of this type with unspecified time-dependent coefficients, no analytical solution to Schrödinger's equation exists [20, 21]. In order to reconstruct the Hamiltonian we make use of two additional features of our experiment. The first is that we can switch off the Hamiltonian at time t_{off} on a timescale which is fast compared to the evolution of the qubit. Secondly we are able to offset one of the terms in the Hamiltonian, in our case by adding a static detuning term $\hat{H}_s = \hbar\delta_L\hat{\sigma}_z/2$ such that the total Hamiltonian is $\hat{H}_I(t) + \hat{H}_s$. We then measure the expectation value of the qubit in the $\hat{\sigma}_z$ basis as a function of δ_L and t_{off} . Repeating the experiment with identical settings many times, we obtain an estimate of the expectation value which we denote as $\langle\hat{\sigma}_z^{\text{meas}}(t_{\text{off}}, \delta_L)\rangle$.

Hamiltonian extraction involves theoretically generating the qubit populations $\langle\hat{\sigma}_z^{\text{sim}}(t_{\text{off}}, \delta_L)\rangle$, and attempting to find the Hamiltonian for which this most closely matches the data. In order to provide a simple parameterization, we represent $\delta(t)$ and $\Omega(t)$ as a linear weighted combination of basis splines [22, 23]. $\langle\hat{\sigma}_z^{\text{sim}}(t_{\text{off}}, \delta_L)\rangle$ is compared to the measured data using a weighted least-squares cost function, which we optimize with respect to the weights of the basis-splines used to parameterize $\delta(t)$ and $\Omega(t)$. Solving this optimization problem in general is hard because the cost function is subject to strong constraints imposed by quantum mechanics, producing a non-trivial relation between the weights and the spin populations [19]. We overcome this problem by making use of the inherent causality of the quantum-mechanical evolution, and by assuming that the parameters of the Hamiltonian vary smoothly. We call our technique “Extending the Horizon Estimation”, in analogy to estab-

lished methods in engineering [24] (a detailed description of our method can be found in [19]). Rather than optimizing over the whole data set at once, we build up the solution by initially fitting the data over a limited region of time $0 < t_{\text{off}} < T_0$. The solution obtained over this first region can be extrapolated over a larger time span $0 < t < T_1$ where $T_1 = T_0 + \tau$, which we use as a starting point to find an optimal solution for this extended region. This procedure is iterated until $T_{n_{\text{max}}} = \max(t_{\text{off}})$. The method allows us to choose a reduced number of basis spline functions to represent $\delta(t)$ and $\Omega(t)$, and also reduces the amount of data considered in the early stages of the fit, when the least is known about the parameters. This facilitates the use of non-linear minimization routines, which are based on local linearization of the problem and converge faster near the optimum. More details regarding the optimization routine can be found in [19].

In the experimental work, we demonstrate reconstruction of the spin Hamiltonian for an ion transported through a near-resonant laser beam. Our qubit is encoded in the electronic states of a trapped calcium ion, which is defined by $|0\rangle \equiv |^2S_{1/2}, M_J = 1/2\rangle$ and $|1\rangle \equiv |^2D_{5/2}, M_J = 3/2\rangle$. This transition is well resolved from all other transitions, and has an optical frequency $\omega_0/(2\pi) \simeq 411.0420$ THz. The laser beam points at 45 degrees to the transport axis, and has an approximately Gaussian spatial intensity distribution. The time-dependent velocity $\dot{z}(t)$ of the ion is controlled by adiabatic translation of the potential well in which the ion is trapped. This is implemented by applying time-varying potentials to multiple electrodes of a segmented ion trap, which are generated using a multi-channel arbitrary waveform generator, each output of which is connected to a pair of electrodes via a passive third order low-pass Butterworth filter. The result is that the ion experiences a time-varying Rabi frequency $\Omega(t)$ and a laser phase which varies with time as $\Phi(t) = \phi(z(t)) - \omega_L t$, where $\phi(z(t)) = k_z(z(t))z(t)$ with $k_z(z(t))$ the laser wavevector projected onto the transport axis at position $z(t)$ and ω_L the laser frequency. The spatial variation of $k_z(z(t))$ accounts for the curvature of the wavefronts of the Gaussian laser beam. In order to create a Hamiltonian of the form of equation 1, we work with the differential of the phase, which gives a detuning $\delta(t) = \delta_L - \dot{\phi} = (k'_z(z)z + k_z(z))\dot{z}$ with $\delta_L = \omega_L - \omega_0$ the laser detuning from resonance. For planar wavefronts $k'_z(z) = 0$, and $\delta(t)$ corresponds to the familiar expression for the first-order Doppler shift (see [19] for details).

The experimental sequence is depicted in figure 1. We start by cooling all motional modes of the ion to $\bar{n} < 3$ using a combination of Doppler and electromagnetically-induced-transparency cooling [25], and then initialize the internal state by optical pumping into $|0\rangle$. The ion is then transported to zone A, and the laser beam used to implement the Hamiltonian is turned on in zone B. The ion is then transported through this laser beam to zone C. During the passage through the laser beam, we rapidly

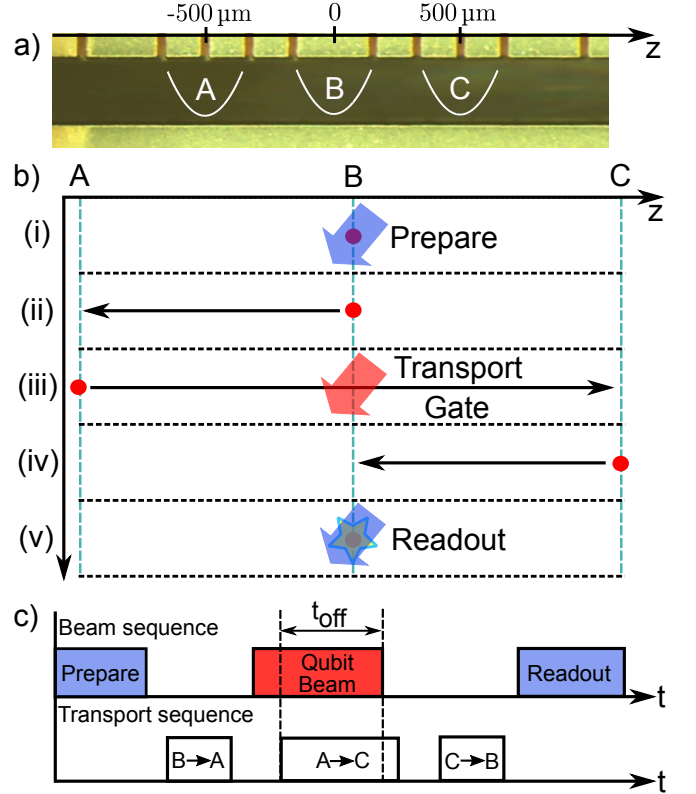


FIG. 1: **Experimental sequence and timing:** a) The experiment is carried out in three zones of the trap indicated by A, B and C. b) The experimental sequence involves steps (i) through (v). Preparation and readout are carried out on the static ion in zone B. The qubit evolves while the ion is transported from zone A to zone C, via the laser beam in zone B. c) Experimental sequence showing the timing of applied laser beams and ion transport, including shutting off the laser beam during transport.

turn the beam off at time t_{off} and thus stop the qubit dynamics. The ion is then returned to the central zone B in order to perform state readout, which measures the qubit in the computational basis (for more details see [19]). The additional Hamiltonian \hat{H}_s is implemented by offsetting the laser frequency used in the experiment by a detuning δ_L . For each setting of t_{off} and δ_L the experiment is repeated 100 times, allowing us to obtain an estimate for the qubit populations $\langle \hat{\sigma}_z(t_{\text{off}}, \delta_L) \rangle$.

Experimental data is shown in figure 2 for two different beam positions, alongside the results of fitting performed using our iterative method. The beam positions used for each data set differ by around 64 μm, but the transport waveform used was identical. The reconstructed velocities should therefore agree in the region where the data overlap. It can be seen from the residuals that the estimation is able to find a Hamiltonian which results in a close match to the data. In order to get an estimate of the relevant error bars for our reconstruction, we have performed non-parametric resampling with replacement, optimizing for the solution using the same set of B-spline

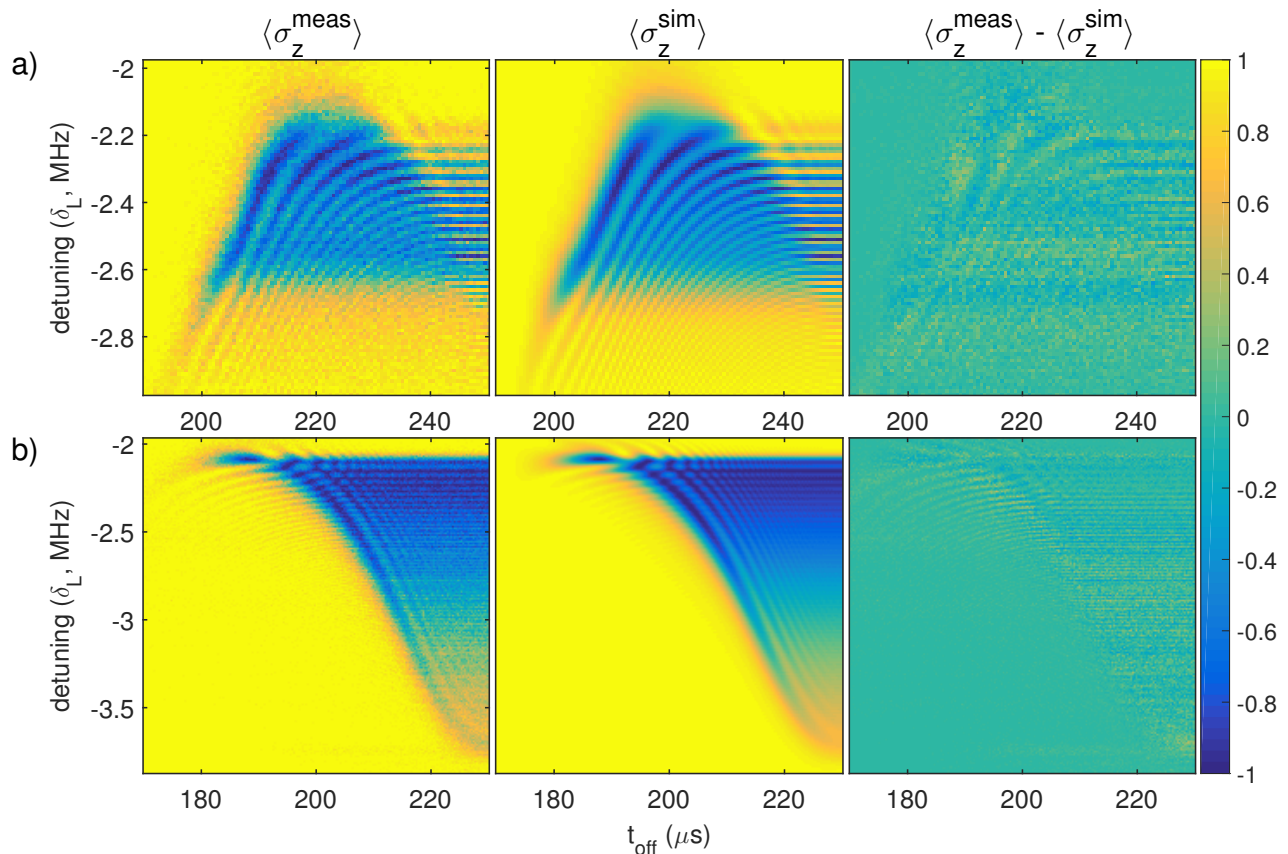


FIG. 2: **Measured data, estimation and residuals:** Spin population as a function of detuning and switch-off time of the laser beam. a) is for a laser beam centered in zone B, while for b) the beam was displaced towards zone C by $64 \mu\text{m}$. From left to right are plotted the experimental data, the populations generated from the best fit Hamiltonian, and the residuals. Each data point results from 100 repetitions of the experimental sequence. The data in a) consist of an array of 100×101 experimental settings, while that shown in b) consists of an array of 201×201 settings. This leads to smaller error bars in the reconstructed Hamiltonian for the latter. For the Hamiltonian estimation the data was weighted according to quantum projection noise.

functions as was used for the experimental data to provide a new estimate for the Hamiltonian. This is repeated for a large number of samples, resulting in a distribution for the estimated values of $\delta(t)$ and $\Omega(t)$ from which we extract statistical properties such as the standard error. The error bounds shown in figures 3 correspond to the standard error on the mean obtained from these distributions (see [19] for further details).

The estimated coefficients of the Hamiltonian extracted from the two data sets are shown in figure 3a). It can be seen that the values of $\delta(t)$ for the two different beam positions differ for the region where the reconstructions overlap. We think that this effect arises from the non-planar wavefronts of the laser beam. Inverting the expression for $\delta(t)$ to obtain the velocity of the ion, we find $\dot{z}(t) = \delta(t)/(k'_z(z)z + k_z(z))$. Using this correction, we find that the two velocity profiles agree if we assume that the ion passes through the center of the beam at a distance of 2.27 mm before the minimum beam waist, a value which is consistent with experimental uncertainties due to beam propagation and possible mis-positioning of

the ion trap with respect to the fixed final focusing lens. The velocity estimates taking account of this effect are shown in figure 3b).

Figure 4 shows the results of a reconstruction for a second pair of data sets taken using two different velocity profiles but with a common beam position. The resolution in both time and detuning were lower in this case than for the data shown in figure 2 (see [19] for the data). We observe that the estimated Rabi frequency profiles agree to within the error bars of the reconstruction. One interesting feature of this plot is that the error bars produced from the resampled data sets are notably higher at the peak than on the sides of the beam. We think that this happens because the sampling time of the data is $0.5 \mu\text{s}$, which is not high enough to accurately resolve the fast population dynamics resulting from the high Rabi frequency (the Nyquist frequency is 1 MHz). In order to optimize the efficiency of our method, it would be advantageous to run the reconstruction method in parallel with data taking, thus allowing updating of the sampling time and frequency resolution of points based on the current

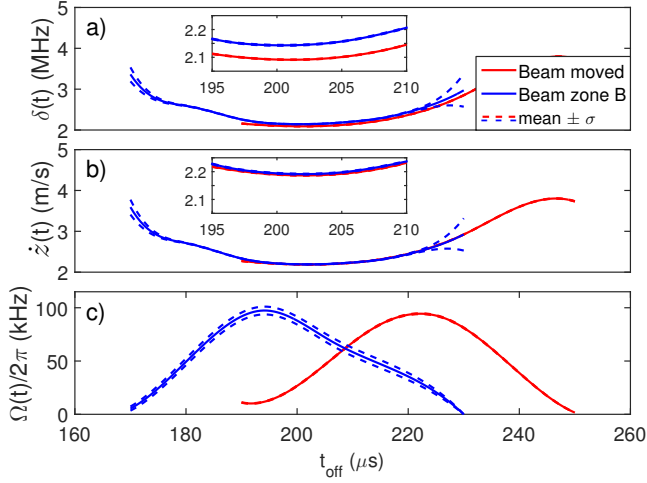


FIG. 3: **Estimates of time-dependent co-efficients:** a) The effective detuning $\delta(t)$ and c) Rabi frequency $\Omega(t)$ obtained from the two data sets, along with dashed lines indicating the standard error on the mean of these estimates obtained from resampling. For a), the inset shows a close up of the estimated $\delta(t)$ in the regions where the estimates overlap, showing that these do not give the same value. b) The estimated velocity $\dot{z}(t)$ of the ion obtained after applying wavefront correction. The inset shows that this can produce consistent results.

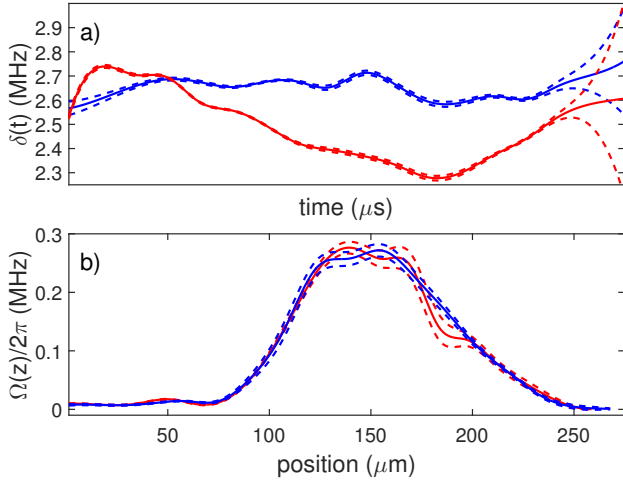


FIG. 4: **Spatial Rabi frequency:** a) The estimated $\delta(t)$ obtained from the second pair of data sets (Figure 8 in [19]). b) The estimated Rabi frequency $\Omega(t)$ for the same two data sets.

estimates of parameter values.

Our method for directly obtaining a non-commuting time-dependent Hamiltonian uses straightforward measurements of the qubit state in a fixed basis as a function of time and a controlled offset to the Hamiltonian. This simplicity means that the method should be applicable in a wide range of physical systems where such control is available, including many technologies considered for quantum computation [1, 5, 6, 26, 27]. A process-tomography based approach would require that for every time step multiple input states be introduced, and a measurement made in multiple bases [28–30]. An effective modulation of the measurement basis arises in our approach due to the additional detuning δ_L . It is worth noting that tomography provides more information than our method: it makes no assumptions about the dynamics aside from that of a completely positive map while we require coherent dynamics. Extensions to our work are required in order to provide a rigorous estimation of the efficiency of the method in terms of the precision obtained for a given number of measurements, and to see whether a similar approach could be taken to non-unitary dynamics. Using this method on considerably lower resolution data sets, we have recently been able to improve the control over the velocity, which will be necessary in order to realize multi-qubit transport gates in our current setup [7].

We thank Lukas Gerster, Martin Sepiol and Karin Fisher for contributions to the experimental apparatus. We acknowledge support from the Swiss National Science Foundation under grant numbers 200021_134776 and 200020_153430, ETH Research grant under grant no. ETH-18 12-2, and from the National Centre of Competence in Research for Quantum Science and Technology (QSIT).

Author Contributions: Experimental data was taken by LdC, RO and MM using apparatus built up by all authors. Data analysis was performed by LdC and RO. The paper was written by JPH, LdC and RO, with input from all authors. The work was conceived by JPH and LdC.

-
- [1] J. Zhang and M.Sarovar. Quantum hamiltonian identification from measurement time traces. *Phys. Rev. Lett.*, 113(080401), 2014.
 - [2] A. Mitra and H. Rabitz. Identifying mechanisms in the control of quantum dynamics through hamiltonian encoding. *Phys. Rev A.*, 67(033407), 2003.
 - [3] R. Rey de Castro and H. Rabitz. Laboratory imple-

- mentation of quantum-control-mechanism identification through hamiltonian encoding and observable decoding. *Phys. Rev A.*, 81(063422), 2010.
- [4] R. Rey de Castro, R. Cabrera, D. I Bondar, and H. Rabitz. Time-resolved quantum process tomography using hamiltonian-encoding and observable-decoding. *New J. Phys.*, 15(025032), 2013.

- [5] S. J. Devitt, J. H. Cole, and L. C. L. Hollenberg. Scheme for direct measurement of a general two-qubit hamiltonian. *Phys. Rev A.*, 73(052317):1–5, 2006.
- [6] A. Shabani, M. Mohseni, S. Lloyd, R. L. Kosut, and H. Rabitz. Estimation of many-body quantum hamiltonians via compressive sensing. *Phys. Rev A.*, 84(012107):1–8, 2011.
- [7] D. Leibfried, E. Knill, C. Ospelkaus, and D. J. Wineland. Transport quantum logic gates for trapped ions. *Phys. Rev. A*, 76:032324, Sep 2007.
- [8] D. J. Wineland, C. Monroe, W. M. Itano, D. Leibfried, B. E. King, and D. M. Meekhof. Experimental issues in coherent quantum-state manipulation of trapped atomic ions. *J. Res. Natl. Inst. Stand. Technol.*, 103:259–328, 1998.
- [9] R. Bowler, J. Gaebler, Y. Lin, T.R. Tan, D. Hanneke, J.D. Jost, J.P. Home, D. Leibfried, and D.J. Wineland. Coherent diabatic ion transport and separation in a multizone trap array. *Phys. Rev. Lett.*, 109:080502, Aug 2012.
- [10] A. Walther, F. Ziesel, T. Ruster, S.T. Dawkins, K. Ott, M. Hettrich, K. Singer, F. Schmidt-Kaler, and U. Poschinger. Controlling fast transport of cold trapped ions. *Phys. Rev. Lett.*, 109:080501, Aug 2012.
- [11] J.M. Martinis and M.R. Geller. Fast adiabatic gates using only σ_z control. *Phys. Rev A.*, 90(022307), 2014.
- [12] R. Schutjens, F. Abu Dagga, D.J. Egger, and F.K. Wilhelm. Single-qubit gates in frequency-crowded transmon systems. *Phys. Rev. A*, 88:052330, Nov 2013.
- [13] J. H. Cole, S. G. Schirmer, A. D. Greentree, C. J. Wellard, D. K. L. Oi, and L. C. L. Hollenberg. Identifying an experimental two-state hamiltonian to arbitrary accuracy. *Phys. Rev A.*, 71(6):1–11, 2005.
- [14] N. Zhao, J. Honert, B. Schmid, M. Klas, J. Isoya, M. Markham, D. Twitchen, F. Jelezko, R-B. Liu, Helmut Fedder, and Jörg Wrachtrup. Sensing single remote nuclear spins. *Nature Nanotech.*, 7:657–662, 2012.
- [15] A. Blais, R.-S. Huang, A. Wallraff, S. M. Girvin, and R. J. Schoelkopf. Cavity quantum electrodynamics for superconducting electrical circuits: An architecture for quantum computation. *Phys. Rev. A*, 69(062320), 2004.
- [16] M. H. Devoret and R. J. Schoelkopf. Superconducting circuits for quantum information: An outlook. *Science*, 339:1169–1174, 2013.
- [17] H. Ball and M. J. Biercuk. Walsh-synthesized noise filters for quantum logic. *EPJ Quantum Technology*, 2(1):1–45, 2015.
- [18] L. de Clercq, H.-Y. Lo, M. Marinelli, D. Nadlinger, R. Oswald, V. Negnevitsky, D. Kienzler, B. Keitch, and J. P. Home. Parallel transport-based quantum logic gates with trapped ions. *arXiv:1509.06624*, 2015.
- [19] Materials and methods are available online.
- [20] E. Barnes and S. Das Sarma. Analytically solvable driven time-dependent two-level quantum systems. *Phys. Rev. Lett.*, 109(060401), 2012.
- [21] E. Barnes. Analytically solvable two-level quantum systems and landau-zener interferometry. *Phys. Rev. A*, 88(013818), 2013.
- [22] R. H. Bartels, J. C. Beatty, and B. Barsky. *An introduction to splines for use in computer graphics and geometric modeling*. Elsevier, 1995.
- [23] Carl de Boor. B(asic)-spline basics. [http://www.researchgate.net/publication/228398058_B_\(asic\)-spline_basics](http://www.researchgate.net/publication/228398058_B_(asic)-spline_basics). Notes that are kept up to date by the author.
- [24] K. R. Muske and J. B. Rawlings, editors. *Methods of Model Based Process Control*. Springer Netherlands, 1995.
- [25] C. F. Roos, D. Leibfried, A. Mundt, F. Schmidt-Kaler, J. Eschner, and R. Blatt. Experimental demonstration of ground state laser cooling with electromagnetically induced transparency. *Phys. Rev. Lett.*, 85(26):5547–5550, 2000.
- [26] R. Barends, L. Lamata, J. Kelly, L. Garcia-Alvarez, A.G. Fowler, A. Megrant, E. Jeffrey, T.C. White, D. Sank, J.Y. Mutus, B. Campbell, Yu Chen, Z. Chen, B. Chiaro, A. Dunsworth, I.-C. Hoi, C. Neill, P.J.J. O’Malley, C. Quintana, P. Roushan, A. Vainsencher, J. Wenner, E. Solano, and John M. Martinis. Digital quantum simulation of fermionic models with a superconducting circuit. *Nat. Commun.*, 6(7654), 2015.
- [27] C. Bonato, M. S. Blok, H. T. Dinani, D. W. Berry, M. L. Markham, D. J. Twitchen, and R. Hanson. Optimized quantum sensing with a single electron spin using real-time adaptive measurements. *arXiv preprint arXiv:1508.03983*, 2015.
- [28] I. L. Chuang and M. A. Nielsen. Prescription for experimental determination of the dynamics of a quantum black box. *J. Mod. Opt.*, 44:2455–2467, 1997.
- [29] J. F. Poyatos, J. I. Cirac, and P. Zoller. Complete characterization of a quantum process: the two-bit quantum gate. *Phys. Rev. Lett.*, 78(2):390–393, 1997.
- [30] M. Riebe, K. Kim, P. Schindler, T. Monz, P. O. Schmidt, T. K. Körber, W. Hänsel, H. Häffner, C. F. Roos, and R. Blatt. Process tomography of ion trap quantum gates. *Phys. Rev. Lett.*, 97:220407, 2006.
- [31] B.E.A. Saleh and M.C. Teich. *Fundamentals of photonics*. Wiley, 2007.
- [32] K. P. Murphy. *Machine learning: a probabilistic perspective*. MIT press, 2012.

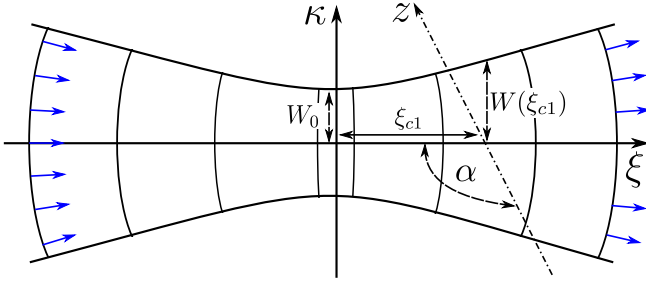


FIG. 5: **Beam and ion transport:** The beam propagation direction lies along the ξ -axis and the ion is transported along the z -axis lying the $\kappa\xi$ -plane as indicated. Normalized vectors representing $\vec{e}_l(\kappa, \xi)$ lying perpendicular to the wavefronts are indicated by the blue arrows.

I. SUPPLEMENTARY MATERIAL

A. Derivation of Hamiltonian

The interaction of a laser beam with frequency ω_L and wave vector $\vec{k}(\vec{z}(t))$ with a two-level atom with resonant frequency ω_0 and time-dependent position of the ion $\vec{z}(t) = (0, 0, z(t))$ can be described in the Schrödinger picture by the Hamiltonian

$$\hat{H}_S = -\frac{\hbar\omega_0}{2}\hat{\sigma}_z - \hbar\Omega(z(t))\cos\left(\vec{k}(\vec{z}(t))\cdot\vec{z}(t) - \omega_L t\right)\hat{\sigma}_x, \quad (2)$$

where the Rabi frequency $\Omega(z(t))$ gives the interaction strength between the laser and the two atomic levels. We can define the laser phase at the position of the ion as $\Phi(t) = \phi(t) - \omega_L t$ with $\phi(t) = \vec{k}(\vec{z}(t))\cdot\vec{z}(t) = k_z(z(t))z(t)$ and $k_z(z(t)) = |\vec{k}|\cos(\theta(t))$ being the projection of the laser beam onto the z -axis along which the ion is transported. Here $\theta(t)$ is the angle between the wave-vector $\vec{k}(z(t))$ and the transport axis evaluated at position $z(t)$. Moving to a rotating frame using the unitary transformation $U = e^{-i\frac{\Phi(t)}{2}}$ and applying the rotating wave approximation with respect to optical frequencies, we obtain

$$\hat{H}_I = \frac{\hbar}{2}\left(-\Omega(t)\hat{\sigma}_x + \left(-\omega_0 - \dot{\Phi}(t)\right)\hat{\sigma}_z\right). \quad (3)$$

Defining a static detuning $\delta_L = \omega_L - \omega_0$ we obtain

$$\hat{H}_I = \frac{\hbar}{2}\left(-\Omega(t)\hat{\sigma}_x + \left(\delta_L - \dot{\phi}(t)\right)\hat{\sigma}_z\right). \quad (4)$$

with

$$\delta(t) = \delta_L - \dot{\phi}(t) \quad (5)$$

which is the expression used in the main text.

B. Wavefront correction

For plane waves we find that $\dot{\phi}(t) = \vec{k} \cdot \vec{v}(t)$ which is the well-known expression for the first-order Doppler

shift. For transport through a real Gaussian beam, the wave-vector direction changes with position. Taking this into account, the derivative of $\phi(t)$ becomes

$$\dot{\phi}(t) = [k'_z(z(t))z(t) + k_z(z(t))] \dot{z}(t) \quad (6)$$

where $k'_z = dk_z/dz$ and $\dot{z}(t)$ is the component of the ion's velocity which lies along the z -axis. We extract $\delta(t)$ using our Hamiltonian estimation procedure, thus to obtain the velocity of the ion we use

$$\dot{z}(t) = \frac{-\delta(t) + \delta_L}{k'_z(z(t))z(t) + k_z(z(t))}. \quad (7)$$

As the ion moves through the beam it experiences the same magnitude of the wave vector $|\vec{k}| = 2\pi/\lambda$, but the angle θ between the ion's direction and the wave vector changes. Written as a function of this angle, the velocity becomes

$$\dot{z}(t) = \frac{-\delta(t) + \delta_L}{-|\vec{k}|\sin(\theta(z(t)))\theta'(z(t))z(t) + |\vec{k}|\cos(\theta(z(t)))} \quad (8)$$

where $\theta'(z(t)) = d\theta(z(t))/dz(t)$. We parameterize our Gaussian beam according to figure 5. The phase is given as a function of both the position along the beam axis ξ and the perpendicular distance from this axis κ by [31]

$$\varphi(\kappa, \xi) = |\vec{k}|\xi - \zeta(\xi) + \frac{|\vec{k}|\kappa^2}{2R(\xi)}. \quad (9)$$

where the Gaussian beam parameters include the beam waist $W(\xi)$, the radius of curvature $R(\xi)$ the Rayleigh range ξ_R and the Guoy phase shift $\zeta(\xi)$. These are given by the expressions

$$\begin{aligned} W(\xi) &= W_0 \sqrt{1 + \left(\frac{\xi}{\xi_R}\right)^2} \\ R(\xi) &= \xi \left(1 + \left(\frac{\xi_R}{\xi}\right)^2\right) \\ \zeta(\xi) &= \tan^{-1}\left(\frac{\xi}{\xi_R}\right) \\ \xi_R &= \frac{\pi W_0^2}{\lambda} \\ k &= \frac{2\pi}{\lambda} \end{aligned} \quad (10)$$

where W_0 is the minimum beam waist and λ the laser wavelength. The ion moves along the z -axis shown in figure 5. In the $\kappa\xi$ -plane a unit vector $\vec{e}_l(\kappa, \xi)$ perpendicular to the wavefronts is given by

$$\vec{e}_l(\kappa, \xi) = \frac{\nabla\varphi(\kappa, \xi)}{\|\nabla\varphi(\kappa, \xi)\|} \quad (11)$$

and the unit vector \vec{e}_v pointing along the direction of transport is given by

$$\vec{e}_v = \begin{bmatrix} \cos(\alpha) \\ \sin(\alpha) \end{bmatrix} \quad (12)$$

The angle $\theta(\xi)$ between the wave and position vector is then given by the dot product

$$\theta(\kappa) = \cos^{-1}(\vec{e}_n \cdot \vec{e}_v). \quad (13)$$

which can be written in terms of the full set of parameters above as

$$\begin{aligned} \theta(\kappa) &= \cos^{-1}(\gamma_1 + \gamma_2) \\ \gamma_1 &= \frac{\cos(\alpha) \left(-2\xi_R (\xi^2 + \xi_R^2) + k\kappa^2 (\xi_R^2 - \xi^2) + 2k (\xi^2 + \xi_R^2)^2 \right)}{\eta(\kappa)} \\ \gamma_2 &= \frac{\sin(\alpha) 2k\kappa\xi (\xi^2 + \xi_R^2)}{\eta(\kappa)} \\ \eta(\kappa, \xi) &= (\xi^2 + \xi_R^2) \left[4 \left(\frac{k\kappa\xi}{\xi^2 + \xi_R^2} \right)^2 + \left(-\frac{2\xi_R}{\xi^2 + \xi_R^2} + k \left(2 + \frac{\kappa^2 (\xi_R^2 - \xi^2)}{(\xi^2 + \xi_R^2)^2} \right) \right)^2 \right] \\ \kappa(t) &= z(t) \sin(\alpha) \end{aligned} \quad (14)$$

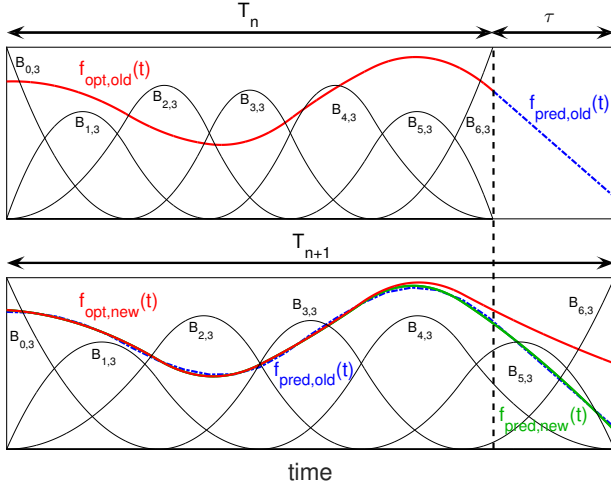


FIG. 6: **Extending the Horizon Estimation:** The steps performed when extending the time horizon from T_n to T_{n+1} are illustrated. We first predict in the old basis, then move to the new basis, and finally optimize again. The figure also shows the basis splines $B_{i,k}(t)$.

where in our experiments $\alpha = 3\pi/4$.

Using Eq. 8 and 14 we examined the value of ξ_{cl} required for the velocity to match for our two beam positions. We find that they agree for $\xi_{cl} = -2.27$ mm, which is within the experimental uncertainties for our setup.

C. Basis spline curves

One challenge in obtaining an estimate for the Hamiltonian is that we must optimize over continuous functions $\delta(t)$ and $\Omega(t)$. To address this, we represent $\delta(t)$

and $\Omega(t)$ with basis spline curves. Basis spline curves allow the construction of smooth functions using only a few parameters. This is achieved by introducing a set of polynomial Basis (B)-spline functions $B_{i,k}(t)$ of order k [23]. A smooth curve $S(t)$ can then be represented as a linear combination of these B-spline basis functions [22]

$$S(t) = \sum_{i=0}^n \alpha_i B_{i,k}(t). \quad (15)$$

The B-splines $B_{i,k}(t)$ of order k are recursively defined over the index i over a set of points $\vec{K} = \{t_0, t_1, \dots, t_{n+k}\}$ which is referred to as the knot vector [23].

$$\begin{aligned} B_{i,1}(t) &= \begin{cases} 1 & t_i \leq t \leq t_{i+1} \\ 0 & \text{otherwise} \end{cases} \\ B_{i,k}(t) &= \omega_{i,k}(t) B_{i,k-1}(t) + (1 - \omega_{i+1,k}(t)) B_{i+1,k-1}(t). \\ \omega_{i,k}(t) &= \begin{cases} \frac{t - t_i}{t_{i+k-1} - t_i} & \text{if } t_i \neq t_{i+k-1} \\ 0 & \text{otherwise} \end{cases} \end{aligned} \quad (16)$$

Figure 6 gives a visualization of the B-splines $B_{i,k}(t)$ and a basis spline curve. The B-spline construction ensures that any linear combination of the B-splines is continuous and has $(k-2)$ continuous derivatives. The knot vector \vec{K} determines how the basis functions are positioned within the interval $[t_0, t_{n+k}]$. We notice that for our Hamiltonian the spacing of the B-splines is not critical, which we think is due to the smoothness of the variations in our Hamiltonian parameters $\delta(t)$ and $\Omega(t)$. We therefore used the Matlab function *spap2* to automatically choose a suitable knot vector and restricted ourselves to optimizing the coefficients α_i . We collect all coefficients α_i for $\delta(t)$ and $\Omega(t)$ and store them in a single vector $\vec{\alpha}$.

D. Extending the Horizon Estimation

The task of inferring the time-dependent Hamiltonian of the form (1) from the measured data can be cast into an optimization problem for which we use a reduced chi-squared cost function

$$J = \frac{1}{\nu} \sum_{t_{\text{off}}} \sum_{\delta_L} \left[\frac{\langle \hat{\sigma}_z^{\text{meas}}(t_{\text{off}}, \delta_L) \rangle - \langle \hat{\sigma}_z^{\text{sim}}(t_{\text{off}}, \delta_L) \rangle}{\sigma^{\text{meas}}(t_{\text{off}}, \delta_L)} \right]^2 \quad (17)$$

where $\nu = N - n - 1$ is the degrees of freedom with N the number of data points and n the number of fitting parameters, and $\sigma^{\text{meas}}(t_{\text{off}}, \delta_L)$ is the standard error on the estimated $\langle \hat{\sigma}_z^{\text{meas}}(t_{\text{off}}, \delta_L) \rangle$ which we obtain assuming quantum projection noise. In our case the Hamiltonian \hat{H}_I (Eq. 1) with offset $\hat{H}_s = \hbar \delta_L \hat{\sigma}_z / 2$ is parametrized by $\Omega(t)$ and $\delta(t)$. We can thus write the problem as

$$\min_{\delta(t), \Omega(t)} J(\delta(t), \Omega(t)) \quad (18)$$

subject to

$$\begin{aligned} i\hbar \frac{\partial}{\partial t} |\Psi(t, \delta_L)\rangle &= (\hat{H}_I(t) + \hat{H}_s) |\Psi(t, \delta_L)\rangle, \\ |\Psi(t=0, \delta_L)\rangle &= |0\rangle, \\ \langle \hat{\sigma}_z^{\text{sim}}(t, \delta_L) \rangle &= \langle \Psi(t, \delta_L) | \hat{\sigma}_z | \Psi(t, \delta_L) \rangle \end{aligned} \quad (19)$$

for all δ_L .

This optimization problem is hard to efficiently solve in general, because it is nonlinear and non-convex due to the nature of Schrödinger's equation and the use of projective measurements. In order to overcome this challenge, we have implemented a method which we call “Extending the Horizon Estimation” (EHE) in analogy to a well-established technique called “Moving Horizon Estimation” (MHE) [24].

The key idea is that because our measurement data arises from a causal evolution, we can also estimate the Hamiltonian in a causal way. We define a time span ranging from the initial time to some later time which we call the time horizon. Instead of optimizing J over the complete time span at once, we first restrict ourselves to a small, initial time horizon reaching only up to the start of the qubit dynamics. Optimizing J over this short time horizon requires fewer optimization parameters and is simpler than attempting to optimize over the full data set. Once we have solved this small sub-problem, we extend the time horizon and re-run the optimization, extrapolating the results of the initial time window into the extended window in order to provide good starting conditions for the subsequent optimization. This is greatly advantageous for the use of non-linear least squares optimization, which typically works by linearizing the problem and converges much faster near the optimum. The extension of the horizon is used repeatedly until the time window covers the full data set.

Conceptually EHE is very similar to MHE. The main difference is that in MHE the time span has a fixed length

and thus its origin gets shifted forwards in time along with the horizon. In EHE the origin stays fixed at the expense of having to increase the time span under consideration. MHE avoids this by introducing a so-called arrival cost to approximate the previous costs incurred before the start of the time span. This keeps the computational burden fixed over time, which is very important as MHE is usually used to estimate the state of a system in real-time, often on severely constrained embedded platforms. Since neither constraint applies to our problem, we decided to extend the horizon rather than finding an approximate arrival cost. This is advantageous since finding the arrival cost in the general case is still an open problem. Due to the similarity between MHE and EHE, we anticipate future improvements by adapting techniques used in MHE to EHE.

Next, we present a more detailed algorithmic summary of our implementation of the method outlined above.

1. Searching for a starting point. Here we reconstruct the Hamiltonian for a first, minimal time horizon such that we can then use this as a starting point to iteratively extend the horizon as described in step 2.

- (a) Choose an initial time horizon such that it contains the region where the first discernible qubit dynamics occur.
- (b) Cut down the number of fitting parameters as much as possible, e.g. by using few Basis splines of low order. This amounts to choosing empirically a low number of basis splines (and thus the length of $\vec{\alpha}_0$) which might represent $\delta(t)$ and $\Omega(t)$ over the given region.
- (c) Use a nonlinear least squares fitting routine to minimize J by varying the parameters $\vec{\alpha}_0$. In the case that the initial fit is not good or no minimum is found, try new initial conditions, change the number of B-spline functions, or manually adjust the function using prior knowledge of the physical system under consideration.

This procedure is used to provide a starting point for the optimization over the initially chosen window, which is typically performed with a higher order set of B-splines. From this starting point, we iteratively extend the fitting method to the full data set as follows.

2. Extend the horizon This step is repeated until the whole time horizon is covered. It consists of the following sequence, which is illustrated in figure 6.

- (a) Extend the time horizon by τ from T_n to $T_{n+1} = T_n + \tau$.
- (b) Extrapolate $f_{\text{opt,old}}(t)$ within τ , e.g. using `fnxtr` in Matlab.

- (c) Adapt the Basis splines to the new time horizon T_{n+1} and represent $f_{\text{pred,old}}(t)$ in the new basis, giving $f_{\text{pred,new}}(t)$. In Matlab one can use *spap2* to do this.
 - (d) Use $f_{\text{pred,new}}(t)$ as the initial guess for a weighted nonlinear least squares fit over the extended time span up to T_{n+1} .
 - (e) Judge the results of the fit based on its reduced chi-squared value χ_{red}^2 . If it is below a specified bound, continue with an additional iteration of steps a)-d), repeating until the full region of the data is covered. Otherwise, try the following fall-back procedures:
 - i. Reduce τ , the time by which the time horizon is extended, and try again
 - ii. Increase the number of Basis splines and try again
 - iii. Try again using a different starting point.
 If all of those fail, we have to resort to increasing the bound on χ_{red}^2 .
3. **Post-processing.** The following steps are optional and were performed manually in cases where we desired to improve the fit, or examine its behaviour.
- (a) The optimization over the whole time horizon was re-run using different numbers of Basis splines for $\delta(t)$ and $\Omega(t)$. This served as a useful check on the sensitivity of the fit.
 - (b) The optimization over the whole time horizon was re-run using a starting point based on the previously found optimum plus randomized deviations. This examines robustness of the final fit.

E. Error estimation

To obtain error bars of the time-dependent functions we use non-parametric bootstrapping [32]. The process is summarized as follow:

1. **Estimate initial solution** Estimate the time dependent functions from the original data using Hamiltonian estimation.
2. **Resampling** Create N_s sample solutions for all time-dependent functions in the following way:
 - (a) Form a sample set by randomly picking with replacement from the photon count data used in qubit detection.
 - (b) Re-estimate new time-dependent functions by optimizing over the full time span, using the solution found in (1) as a starting point.
 - (c) Record the reduced chi-squared values $\chi_{\text{red},r}^2$ for each sample r along with the B-spline curve coefficients $\vec{\alpha}_r$.

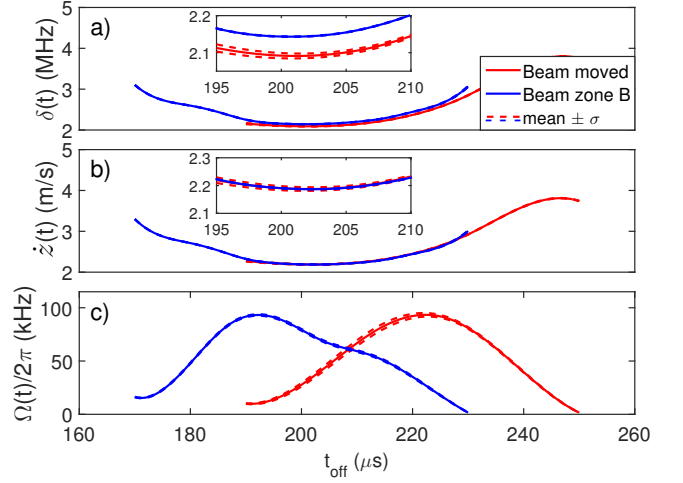


FIG. 7: **Parametric bootstrap resampling:** Predictions for $\delta(t)$, $\dot{z}(t)$ and $\Omega(t)$ with error bounds obtained using parametric bootstrap resampling, assuming quantum projection noise. This can be compared with the error bounds obtained from the non-parametric method which are shown in Figure 3 in the main text. The bounds are tighter for the parametric bootstrapping.

3. Post-process samples

- (a) Form a histogram of the chi-squared values $\chi_{\text{red},r}^2$.
- (b) Find and fit a normal-like distribution to the histogram with preference to the spread with lowest lying $\chi_{\text{red},r}^2$ in the case of a multi-modal distribution. From the fit obtain the mean reduced-chi squared value $\langle \chi_{\text{red},r}^2 \rangle$ as well as the standard deviation σ_χ .
- (c) Eliminate the outlier samples by removing all $\vec{\alpha}_r$ with $\chi_{\text{red},r}^2$ values that are $3-5\sigma_\chi$ from the mean $\langle \chi_{\text{red},r}^2 \rangle$.
- (d) Form a matrix \mathbf{Y} where each row vector is a sample set of coefficients $\vec{\alpha}_r$ that remained after step 3(c).

4. Obtain statistics

- (a) Find the mean B-spline coefficients $\langle \vec{\alpha} \rangle$ of equation 15 by taking the mean over the column vectors of \mathbf{Y} with each element of the mean given by $\langle \vec{\alpha} \rangle_i = \langle \alpha_i \rangle$.
- (b) Find the covariance matrix $\Sigma = \text{cov}(\mathbf{Y}^\alpha)$ with $\Sigma_{ij} = \text{E}[(\alpha_i - \langle \alpha_i \rangle)(\alpha_j - \langle \alpha_j \rangle)]$ with E the expectation operator. The standard deviations of each of the mean coefficients $\langle \alpha_i \rangle$ is given by $\sigma_{\langle \alpha_i \rangle} = \sqrt{\Sigma_{ii}}$. We record these values in a row vector $\vec{\sigma}_{\langle \alpha_i \rangle}$.

We have also applied parametric bootstrapping in order to obtain the error bounds shown in figure 7. The difference to the non-parametric case is that in point (2)

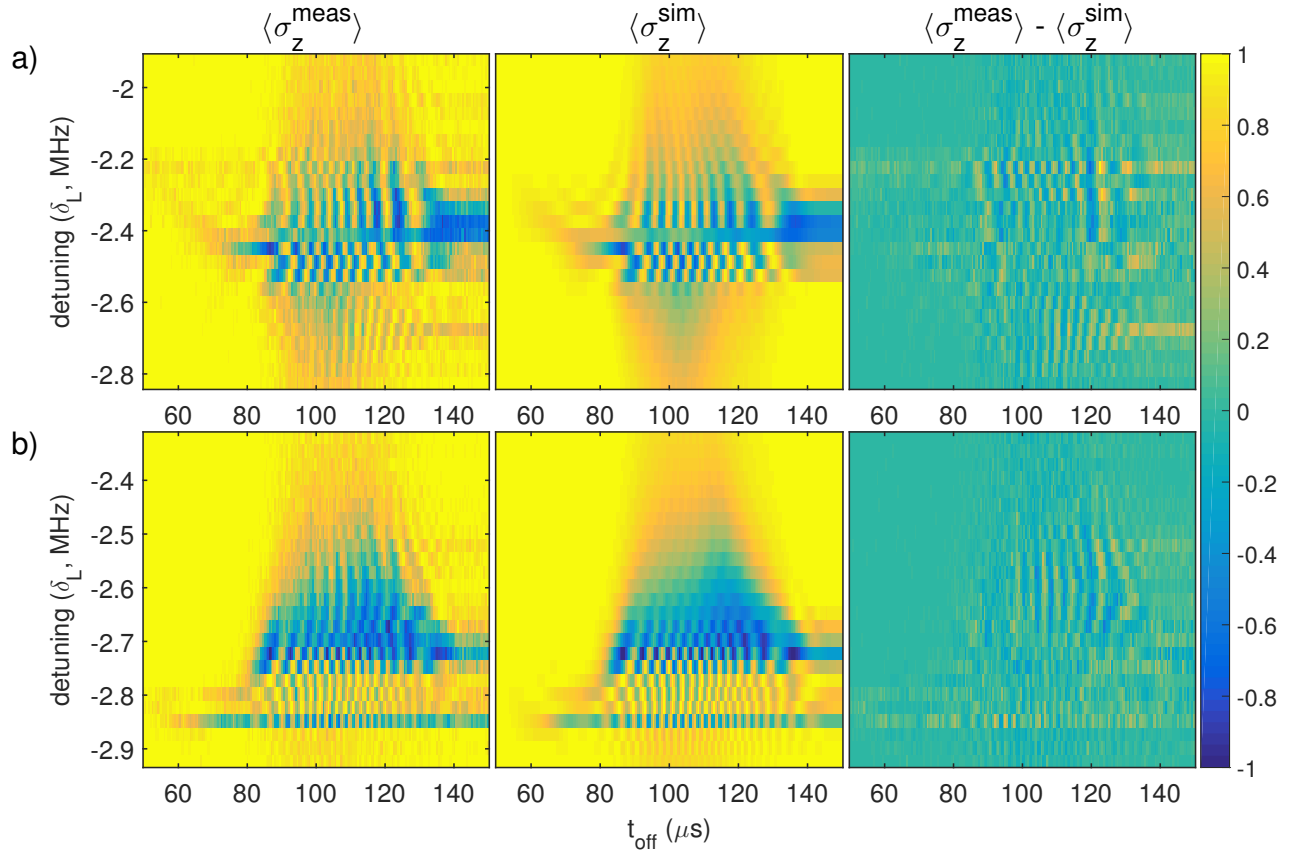


FIG. 8: **Measured data, estimation and residuals:** Spin population as a function of detuning and switch-off time of the laser beam, for the data sets used to obtain the reconstructed parameters shown in figure 4. a) uses a velocity profile with only small variations. b) A second data run in which large variations in the velocity profile were used. Each data point results from 100 repetitions of the experimental sequence. For the Hamiltonian estimation the data was weighted according to quantum projection noise.

the samples are created using the solutions obtained from (1) and adding quantum projection noise. For each sample the Hamiltonian is estimated. The estimates from multiple samples are used to construct error bounds in the same manner as for the non-parametric resampling. We have found that the error bounds obtained from parametric bootstrapping are lower compared to that of the non-parametric case as shown in figure 3. We think this is due to the latter exploring deviations around a single minimum in the optimization landscape, while the case resampling arrives at different local minima which are spread over a wider region.

F. Single beam profile with two different velocity profiles.

As a check that our method is also able to produce consistent results for the Rabi frequency profile, we measured

a second pair of data sets in which we take two different velocity profiles using the same beam position. This data is shown in Figure 8. Also shown are the best-fits obtained from the reconstructed Hamiltonians. The parameter variations obtained from the reconstructed Hamiltonians for these data sets can be found in the main text in Figure 4. The sampling rate of the data in these data sets was 2 MHz, resulting in a Nyquist frequency of 1 MHz.